

Particle Acceleration by Pickup Process Upstream of Relativistic Shocks

MASANORI IWAMOTO,¹ TAKANOBU AMANO,² YOSUKE MATSUMOTO,³ SHUICHI MATSUKIYO,¹ AND MASAHIRO HOSHINO²

¹*Faculty of Engineering Sciences, Kyushu University, 6-1, Kasuga-koen, Kasuga, Fukuoka, 816-8580, Japan*

²*Department of Earth and Planetary Science, University of Tokyo, 7-3-1 Hongo, Bunkyo-ku, Tokyo 113-0033, Japan*

³*Department of Physics, Chiba University, 1-33 Yayoi, Inage-ku, Chiba, Chiba 263-8522, Japan*

(Accepted ApJ)

ABSTRACT

Particle acceleration at magnetized purely perpendicular relativistic shocks in electron-ion plasmas are studied by means of two-dimensional particle-in-cell simulations. Magnetized shocks with the upstream bulk Lorentz factor $\gamma_1 \gg 1$ are known to emit intense electromagnetic waves from the shock front, which induce electrostatic plasma waves (wakefield) and transverse filamentary structures in the upstream region via the stimulated/induced Raman scattering and the filamentation instability, respectively. The wakefield and filaments inject a fraction of incoming particles into a particle acceleration process, in which particles are once decoupled from the upstream bulk flow by the wakefield, and are picked up again by the flow. The picked-up particles are accelerated by the motional electric field. The maximum attainable Lorentz factor is estimated as $\gamma_{max,e} \sim \alpha\gamma_1^3$ for electrons and $\gamma_{max,i} \sim (1 + m_e\gamma_1/m_i)\gamma_1^2$ for ions, where $\alpha \sim 10$ is determined from our simulation results. α can increase up to γ_1 for weakly magnetized shock if γ_1 is sufficiently large. This result indicates that highly relativistic astrophysical shocks such as external shocks of gamma-ray bursts can be an efficient particle accelerator.

Keywords: Shocks — Plasma physics— Cosmic rays — High energy astrophysics

1. INTRODUCTION

Particle acceleration is a ubiquitous physical process in the universe. The nonthermal emission spectra of high-energy astrophysical objects such as jets from active galactic nuclei (AGNs) and gamma-ray bursts (GRBs) are generally modeled as the synchrotron and inverse Compton emission of relativistic electrons (see, e.g., Piran 2005; Blandford et al. 2019). AGN jets and GRBs are often invoked for the source of ultra-high-energy cosmic rays (UHECRs) with energies beyond 10^{18} eV (e.g., Hillas 1984). Although the origin of UHECRs is still unknown, recent observations favor the extragalactic origin (Aab et al. 2018; Aartsen et al. 2018). Such astrophysical objects are usually associated with relativistic shocks as a consequence of interaction between jets and interstellar medium. Relativistic shocks are assumed to be an efficient particle accelerator.

Coherent emission of electromagnetic waves from the shock front is intrinsic to relativistic shocks, which has been confirmed by one-dimensional (1D; Langdon et al. 1988; Gallant et al. 1992; Hoshino et al. 1992; Amato & Arons 2006; Plotnikov & Sironi 2019), two-dimensional (2D; Iwamoto et al. 2017, 2018; Plotnikov et al. 2018; Babul & Sironi 2020), and three-dimensional (3D; Sironi et al. 2021) particle-in-cell (PIC) simulations in pair plasmas. It results from the synchrotron maser instability (SMI) in the shock-transition, which is driven by electrons reflected off the shock-compressed magnetic field (Hoshino & Arons 1991). The excited electromagnetic waves whose group velocities are faster than the shock can propagate through the upstream plasmas as precursor waves. The SMI, which is called cyclotron maser instability in weakly relativistic context, is also known as the emission mechanism of coherent radio sources such as auroral kilometric radiation in the Earth and Jovian decametric radiation (see, e.g., Melrose 2017). Recently, some models of fast radio burst based on the coherent emission from relativistic shock via the SMI have been proposed (e.g., Lyubarsky 2014; Beloborodov 2017; Met-

zger et al. 2019; Beloborodov 2020; Margalit et al. 2020) and the SMI in the context of relativistic shocks attracts more attention from astrophysics. The precursor waves excited by the SMI can be strong enough to induce filamentation instability (FI) which is a transverse self-modulation of an intense electromagnetic wave (Kaw et al. 1973; Drake et al. 1974; Max et al. 1974; Sobacchi et al. 2020). The previous multidimensional simulations indeed demonstrated that the intense electromagnetic waves propagating through upstream plasma induce the transverse filamentary structures. The nonlinear effect of the electromagnetic waves plays a significant role in astrophysical plasmas (see also Lyubarsky 2018, 2019).

In electron-ion plasmas, the nonlinear interactions between the precursor waves and the upstream plasmas become more complicated. The stimulated/induced Raman scattering (SRS), which is a parametric decay of an intense electromagnetic wave into an electrostatic plasma wave such as a Langmuir wave, can work in addition to the FI (see, e.g., Kruer 1988; Lyubarsky 2008). This plasma wave is conventionally called wakefield and the concept of the direct particle acceleration by the wakefield via the Landau resonance, which is so-called wakefield acceleration (WFA), is first proposed in the study of laboratory plasmas (Tajima & Dawson 1979). The application of the WFA to the UHECR acceleration is discussed later in the context of astrophysics (e.g., Chen et al. 2002; Arons 2003; Murase et al. 2009; Ebisuzaki & Tajima 2014, 2021) and laboratory plasmas (e.g., Kuramitsu et al. 2008, 2011a,b, 2012; Liu et al. 2017, 2018, 2019). In relativistic shocks, Lyubarsky (2006) first found the wakefield excitation via the SRS using 1D PIC simulations and recent 2D PIC simulations (Sironi & Spitkovsky 2011; Ligorini et al. 2021a,b) confirmed that. Furthermore, 1D PIC simulations by Hoshino (2008) demonstrated that nonthermal electrons and ions are generated in the upstream. Although our high-resolution 2D PIC simulations (Iwamoto et al. 2019) showed that this particle acceleration associated with the wakefield operates even in a 2D system, the detailed acceleration mechanism was not fully understood because it has some different aspects from the standard WFA in laboratory plasmas.

In this work, we investigate the acceleration mechanism in more detail and show that the energetic particles are generated by a pickup process, where some incoming particles are decoupled once from the upstream bulk flow by the wakefield and then accelerated by the motional electric field after picked up by the flow. In an ideal case, the maximum Lorentz factor may reach $\gamma_{max,e} \sim \alpha\gamma_1^3$ for electrons and $\gamma_{max,i} \sim (1 + m_e\gamma_1/m_i)\gamma_1^2$ for ions, where $\alpha \sim 10$ is the factor determined from our simu-

lation results and γ_1 is the upstream bulk Lorentz factor. Although the observed Lorentz factor is smaller than this theoretical estimate due to the limitation of the simulation time, the partial trajectories of energetic particles are well-described by the pickup process. This efficient acceleration process may operate in highly relativistic astrophysical shocks.

2. SIMULATION SETUP

We perform 2D simulations of perpendicular relativistic shocks in electron-ion plasmas by using a fully kinetic electromagnetic PIC code (Matsumoto et al. 2013, 2015), which suppresses the numerical Cherenkov instability by choosing a magic CFL number and enables accurate and stable calculation (Ikeya & Matsumoto 2015). Our basic configuration is illustrated in Figure 1. We consider a rectangular computational domain in the x - y plane with the periodic boundary condition applied in the y direction. The number of grids in each direction is $N_x \times N_y = 80,000 \times 1,536$. The number of particles per cell per species in the upstream and the grid size are respectively set as $N_1\Delta x^2 = 64$ and $\Delta x/(c/\omega_{pe}) = 1/40$, which are motivated by the numerical convergence study of our previous simulations (see Iwamoto et al. 2017, Appendix A). c is the speed of light and ω_{pe} is the proper electron plasma frequency:

$$\omega_{pe} = \sqrt{\frac{4\pi N_1 e^2}{\gamma_1 m_e}}. \quad (1)$$

The time step is automatically determined as $\omega_{pe}\Delta t = 1/40$ because the magic CFL number is $c\Delta t/\Delta x = 1$ for our implicit Maxwell solver. Note that the implicit Maxwell solver is not restricted by the CFL number and thus $c\Delta t/\Delta x = 1$ is numerically stable. A cold ion-electron flow with the ion-to-electron mass ratio $m_i/m_e = 50$ is injected from the right-hand boundary and propagating $-x$ direction with the bulk Lorentz factor γ_1 . Our shock simulations are performed for the two cases: $\gamma_1 = 40$ and 100. The incoming particles are reflected off at the left-hand conducting-wall boundary and trigger the shock propagating $+x$ direction. Our simulation frame corresponds to the downstream rest frame. We focus on purely perpendicular shocks and the upstream ambient magnetic field B_1 is in the z direction.

The basic structure and coherent emission of relativistic magnetized shocks are well-characterized by the ratio of the Poynting flux to the upstream bulk kinetic energy flux:

$$\sigma_s = \frac{B_1^2}{4\pi\gamma_1 N_1 m_s c^2} = \frac{\omega_{cs}^2}{\omega_{ps}^2}, \quad (2)$$

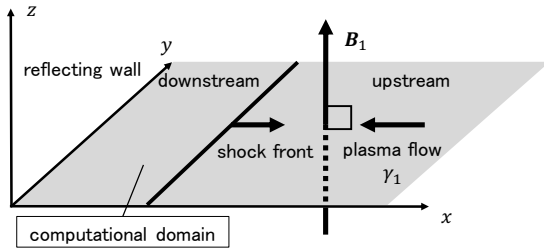


Figure 1. Coordinate system and simulation geometry.

where subscript $s = e, i$ represents the particle species and ω_{cs} is the relativistic cyclotron frequency:

$$\omega_{cs} = \frac{eB_1}{\gamma_1 m_s c}. \quad (3)$$

We use fixed values of $\sigma_i = 0.1$ and $\sigma_e = (m_i/m_e)\sigma_i = 5$ throughout this study.

3. SHOCK STRUCTURE

Figure 2 shows the global shock structures at $\omega_{pe}t = 2000$ in the case of $\gamma_1 = 40$ (left) and 100 (right). The electron number density N_e , the ion number density N_i , the out-of-plane magnetic field B_z , the longitudinal electric field E_x , the longitudinal electric field averaged over the y direction $\langle E_x \rangle$, and the phase space densities in $x-u_{xs}$ and $x-u_{ys}$ for both electrons and ions are shown from top to bottom. All quantities are normalized by the corresponding upstream values and the electron four velocity $\mathbf{u}_e = \gamma_e \boldsymbol{\beta}_e$ are scaled by the mass ratio m_e/m_i . The global structures are similar to each other and show no clear γ_1 dependence.

The clear transverse density filaments are observed in the upstream region as in the case of pair plasmas (Iwamoto et al. 2017, 2018; Plotnikov et al. 2018; Babul & Sironi 2020; Sironi et al. 2021). One might think that the filaments are attributed to the Weibel instability (Weibel 1959; Fried 1959). However, it cannot arise for such high magnetization $\sigma_i = 0.1$ (see, e.g., Spitkovsky 2005; Sironi & Spitkovsky 2011; Sironi et al. 2013). We think that the large-amplitude precursor waves, which are clearly seen in B_z , induce the FI (Kaw et al. 1973; Drake et al. 1974; Max et al. 1974; Sobacchi et al. 2020) and create the filaments. It requires intense electromagnetic pump waves. Actually, the precursor wave amplitude is large in the sense that the wave strength parameter a is greater than unity (Iwamoto et al. 2017; Plotnikov & Sironi 2019):

$$a = \frac{e\delta E}{m_e c \omega} \sim \gamma_1 \sqrt{\epsilon_p} > 1, \quad (4)$$

for $\gamma_1 \gg 1$. Here δE is the wave amplitude, ω is the wave frequency, and $\epsilon_p = \delta B^2/4\pi\gamma_1 N_1 m_e c^2$ is the normalized

precursor wave energy. $\epsilon_p \sim 1$ for $\sigma_i = 0.1$ (Iwamoto et al. 2019) and thus $a \sim \gamma_1 \gg 1$. Therefore, the precursor waves are subject to the FI. The FI is a nonlinear wave-wave interaction and a kind of the parametric decay instability. An intense electromagnetic pump wave with the wave number \mathbf{k}_0 parametrically decays into a compressional wave such as a magnetosonic wave with the wave number \mathbf{k}_1 and two forward-scattered electromagnetic waves with the wave number $\mathbf{k}_2 = \mathbf{k}_0 \pm \mathbf{k}_1$. The beating of these electromagnetic waves operates when $k_1 \ll k_0$ is satisfied. Consequently, the amplitude modulation is induced, which in turn enhances the compressional wave via the ponderomotive force. This self-modulation can occur in the direction perpendicular to the pump wave ($\mathbf{k}_1 \perp \mathbf{k}_0$), resulting in the filaments. Note that this simulation frame corresponds to the downstream rest frame. The filaments are elongated in the x direction due to the Lorentz boost and become more prominent.

The large-scale electrostatic wave (i.e., wakefield) is generated by the SRS in the upstream. The SRS is a kind of the parametric decay instability as well. An intense electromagnetic pump with $\tilde{\mathbf{k}}_0$ parametrically decays into the wakefield with $\tilde{\mathbf{k}}_1$ and a scattered electromagnetic wave with $\tilde{\mathbf{k}}_2 = \tilde{\mathbf{k}}_0 - \tilde{\mathbf{k}}_1$ in the linear phase of the SRS (Hoshino 2008). The sinusoidal wakfield in the far upstream region is induced in this linear phase and particles are merely oscillating as can be seen in the phase space plots. The wakefield gradually get turbulent, indicating the SRS enter the nonlinear phase. Both electrons and ions are strongly accelerated/heated near the shock front. Note that the Lorentz transformation from the proper frame into the simulation frame increases the thermal spread only in the u_x direction. The phase space plots $x-u_{ys}$ show that electrons (ions) are preferentially accelerated in the $+y$ ($-y$) direction. This is because particles are mainly accelerated by the motional electric field $E_y = -\beta_1 B_1$ as discussed in Section 5. These features are consistent with the previous 1D simulation by Hoshino (2008).

4. PARTICLE ENERGY SPECTRA

Figure 3 shows energy spectra of electrons (blue) and ions (red) at $\omega_{pe}t = 2000$ for $\gamma_1 = 40$ (top panels) and $\gamma_1 = 100$ (bottom panels), which are normalized as follows:

$$\int_1^\infty f_s d\gamma = 1. \quad (5)$$

The electron Lorentz factor is scaled by the mass ratio m_e/m_i . The spectra (a), (b), (d), and (e) are measured in the simulation frame. No clear nonthermal tail is seen in the downstream energy spectra (a) and (d)

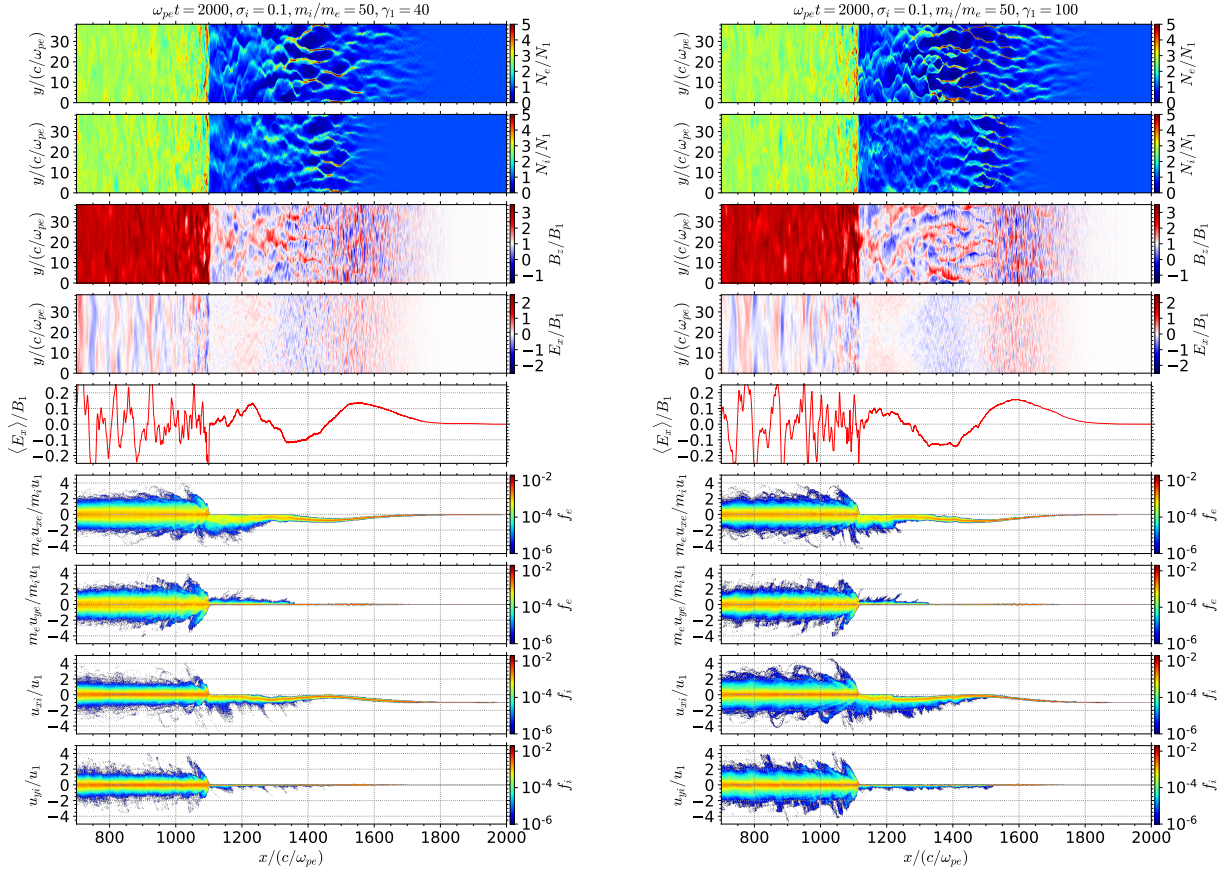


Figure 2. Shock structures at $\omega_{pe}t = 2000$ with $\gamma_1 = 40$ (left) and 100 (right). The electron number density N_e , the ion number density N_i , the z component of the magnetic field B_z , the x component of the electric field E_x , the transversely averaged electric field $\langle E_x \rangle$, and the phase space densities in the $x-u_x$ and $x-u_y$ are shown.

in the range $700 \leq x/(c/\omega_{pe}) \leq 1050$. As can be seen in the near-upstream energy spectra (b) and (e) in the range $1120 \leq x/(c/\omega_{pe}) \leq 1200$, an energy equipartition between electrons and ions is already achieved in the upstream due to the electron-ion coupling via the wakefield (Lyubarsky 2006; Hoshino 2008; Iwamoto et al. 2019). The typical Lorentz factor can be estimated as $\gamma_i = \gamma_e m_e/m_i \sim \gamma_1/2$ and the peaks of the spectra (a), (b), (d), and (e) are roughly consistent with this estimate.

We also show the upstream spectra measured in the plasma rest frame (c) and (f). The prime indicates physical quantities measured in the proper frame. We determined the mean bulk velocity in the region: $1120 \leq x/(c/\omega_{pe}) \leq 1200$ and performed Lorentz transformation into the plasma rest frame. A power-law distribution $\propto \gamma^{-2}$, which is reported in the previous laser plasma experiments and simulations of the WFA (Kuramitsu et al. 2008, 2011a,b, 2012; Liu et al. 2017, 2018, 2019), is also shown in black dashed lines for comparison. The nonthermal electrons and ions are clearly vis-

ible for both γ_1 . These particles are generated by the pickup process as discussed in Section 5

5. ACCELERATION MECHANISM

5.1. Electron acceleration

Here we discuss the electron acceleration mechanism. Figure 4 shows electron trajectories measured in the simulation frame for $\gamma_1 = 40$ in the $x-y$ (top) and $x-\gamma$ (bottom) space. Typical nonthermal and thermal electrons are shown in the red and gray lines, respectively. The thermal electron is merely oscillating within the wakefield. It finally enters the shock at $x/(c/\omega_{pe}) \sim 1080$ and gyrates in the downstream region. The bulk Lorentz factor of the thermal electrons has its maximum when the energy equipartition between ions and electrons is achieved (Lyubarsky 2006; Hoshino 2008; Iwamoto et al. 2019) and thus it is written as

$$\gamma_{max,e}^{th} \sim \frac{1}{2} \frac{m_i}{m_e} \gamma_1. \quad (6)$$

As can be seen in the gray line in Figure 4, the normalized maximum Lorentz factor is $m_e \gamma_e / m_i \gamma_1 \sim 1$.

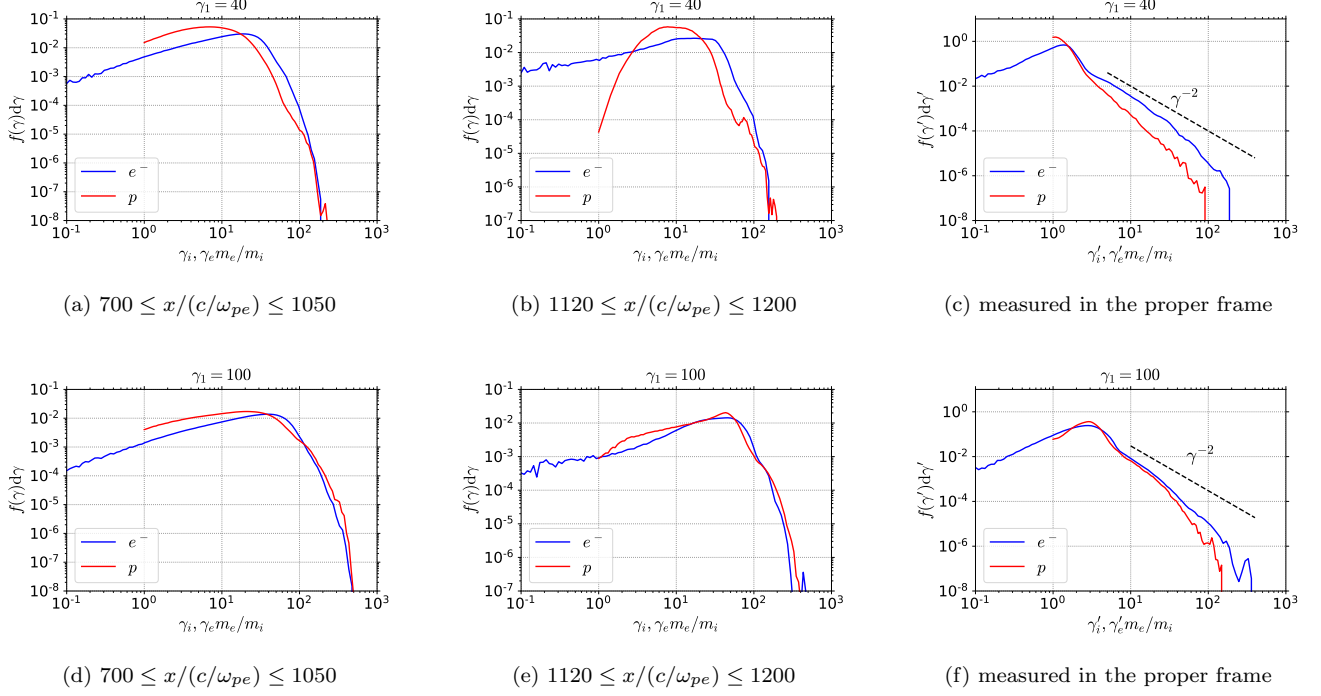


Figure 3. Energy spectra of electrons (blue) and ions (red) for $\gamma_1 = 40$ (top panels) and $\gamma_1 = 100$ (bottom panels). The downstream spectra (left panels), the upstream spectra (middle panels), and the upstream spectra measured in the proper frame (right panels) are shown.

The difference is at most a factor of 2 and this result is roughly consistent with the above estimate. However, the maximum Lorentz factor of the nonthermal electron is much larger and can not be explained by the ion-electron coupling. Although the nonthermal electron is also oscillating in the region: $1230 \lesssim x/(c/\omega_{pe}) \lesssim 1400$, it begins to travel along the $+y$ direction at $x/(c/\omega_{pe}) \sim 1230$ and seems to gain the energy from the motional electric field $E_y = -\beta_1 B_1$. This particle acceleration continues until the electron enters the shock at $x/(c/\omega_{pe}) \sim 1080$. Its maximum Lorentz factor $\gamma_{max,e}$ can be calculated as

$$\gamma_{max,e} = \frac{e\beta_1 B_1 \Delta y}{m_e c^2} = \gamma_1 \beta_1 \sqrt{\sigma_e} \frac{\Delta y}{c/\omega_{pe}}. \quad (7)$$

We measured $\Delta y/(c/\omega_{pe}) \sim 85$ in the region: $1230 \lesssim x/(c/\omega_{pe}) \lesssim 1400$, and thus $m_e \gamma_{max,e}/m_i \gamma_1 \sim 4$, showing a good agreement with our simulation result. This acceleration process is identical to the pickup process in space physics (e.g., Möbius et al. 1985; Oka et al. 2002). In the heliosphere, some neutrals are ionized mainly through charge exchange with solar wind protons and picked up by the solar wind electric field. The pickup ions are efficiently accelerated by the motional electric field. The pickup process including the relativistic effect can be theoretically analyzed using the relativistic equations of motion. We have neglected the precursor

waves, wakefields, and filaments and considered only the ambient magnetic field $B_z = B_1$ and the motional electric field $E_y = -\beta_1 B_1$. The analytical solution in the simulation frame is written as (see Appendix A for the detailed calculations)

$$\gamma_s = \gamma_1^2 \gamma_{0s} [(1 + \beta_1 \beta_{0s}) - \beta_1 (\beta_1 + \beta_{0s}) \cos \theta_s], \quad (8)$$

$$x_s = x_{0s} - c\beta_1 t + \gamma_{0s} (\beta_1 + \beta_{0s}) \frac{c}{\omega_{cs}} \sin \theta_s, \quad (9)$$

$$y_s = y_{0s} \pm \gamma_1 \gamma_{0s} (\beta_1 + \beta_{0s}) \frac{c}{\omega_{cs}} (1 - \cos \theta_s), \quad (10)$$

$$\theta_s = \frac{\omega_{cs} [t + \beta_1 (x_s - x_{0s})/c]}{\gamma_{0s} (1 + \beta_1 \beta_{0s})}, \quad (11)$$

where the subscript 0 indicates the initial quantities at the time when the particles are picked up by the upstream bulk flow. The positive (negative) sign in Equation 10 corresponds to electrons (ions). Here we assume $\beta_{0s} = +\beta_{0s} \hat{x}$. Note that the upstream bulk flow propagates toward the $-x$ direction and ω_{cs} is the unsigned cyclotron frequency. We determined the initial quantities: x_{0s} , y_{0s} , and β_{0s} from our simulations and the theoretical solutions are shown in Figure 4 by the black dashed lines. The simulation results give a good agreement with the theoretical trajectories for the region: $1080 \lesssim x/(c/\omega_{pe}) \lesssim 1240$, indicating that the nonthermal electron is picked up by the bulk flow. The electron reaches the shock front at $x/(c/\omega_{pe}) \sim 1080$

and gradually deviates from the theoretical trajectories. According to Equation 8, the maximum Lorentz factor is estimated as

$$\gamma_{max,s} \sim \gamma_1^2 \gamma_{0s}. \quad (12)$$

Here we have neglected the factors on the order of unity.

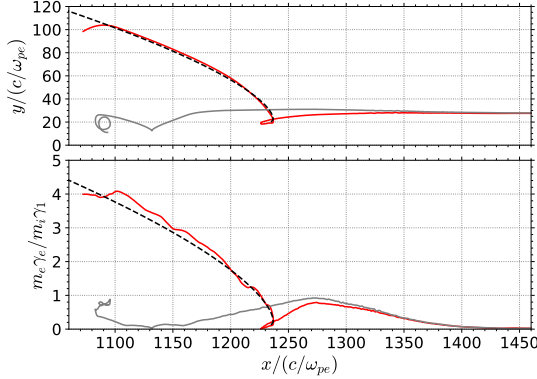


Figure 4. Nonthermal (red) and thermal (gray) electron trajectories in the x - y (top) and x - γ (bottom) space. The black dashed line is the analytical solutions of the pickup process.

The above analytical solution indicates that the nonthermal particles must travel in the opposite direction of the bulk flow before entering into the pickup process. Sironi & Spitkovsky (2011) reported the same acceleration process and pointed out that such particles are decoupled from the bulk flow and thus they can feel the motional electric field due to the velocity difference. Equation 8 indeed demonstrates that the particle acceleration does not occur ($\gamma_s \sim \gamma_1$) for the particle moving with the same velocity as the bulk flow $\beta_{0s} \sim -\beta_1$. Figure 5 shows the trajectories of nonthermal electrons measured in the simulation frame in the gray lines. The color map represents the magnetic field \tilde{B}_z at $\omega_{pe}t = 1800$, which satisfies

$$\tilde{E}_y = -\beta_1 B_1 - \frac{\partial \phi}{\partial y}, \quad (13)$$

$$\tilde{E}_y + \beta_1 \tilde{B}_z = 0. \quad (14)$$

The electrostatic potential ϕ is calculated from the snapshot at $\omega_{pe}t = 1800$ by performing the Helmholtz's decomposition. We have removed the electromagnetic fields arising from the precursor waves because such superluminal waves are not responsible for the resonant wave-particle interaction and do not directly contribute to the particle acceleration. The trajectories in Figure 5 indeed demonstrate that nonthermal electrons propagate toward the $+x$ direction before picked up by the bulk flow. The nonthermal electrons come in to the

weakly magnetized region resulting from the FI and then enters the acceleration phase, indicating that the filaments trigger the pickup process.

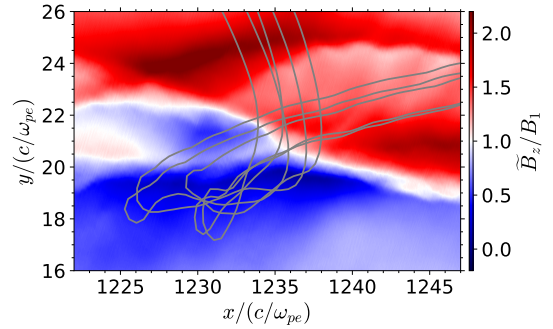


Figure 5. Trajectories of the nonthermal electrons with \tilde{B}_z at $\omega_{pe}t = 1800$.

Figure 6 shows the time evolution of the typical nonthermal electron measured in the simulation frame. We take the moving average for the time period $\omega_{pe}\Delta t = 5$, which is motivated by the typical frequency of the precursor waves: $\omega/\omega_{pe} \sim 2-5$ (Iwamoto et al. 2017, 2018), to remove the effect of the precursor waves. The top panel displays the energy gain $\Delta\gamma_e = \gamma_e - \gamma_1$ (red) and work done by E_x (green) and E_y (blue) normalized by $m_i\gamma_1/m_e$:

$$\Delta\gamma_k = -\frac{e}{m_e c^2} \int_{t_0}^t E_k v_k dt, \quad (15)$$

where $k = x, y$ and $\omega_{pe}t_0 = 1500$. The incoming electron is decelerated by the wakefield and begin to gyrate. Then it loses its energy due to both the wakefield and the motional electric field for $1750 \lesssim \omega_{pe}t \lesssim 1795$. $\Delta\gamma_x$ increases in time for $1795 \lesssim \omega_{pe}t \lesssim 1810$, whereas $\Delta\gamma_y$ is almost constant, showing that the energy gain during the corresponding time period originates from the wakefield. After $\omega_{pe}t \simeq 1810$, $\Delta\gamma_y$ becomes dominant and thus the nonthermal electron enters the pickup process. The x and y components of the electron velocity normalized by the speed of light: β_x (green) and β_y (blue) are shown in the middle panel. β_x is positive for $1795 \lesssim \omega_{pe}t \lesssim 1810$ and the nonthermal electron moves with the relativistic velocity $\beta_x \sim 1$ in the same direction of the wakefield propagation. Note that the phase velocity of the wakefield is almost equal to the speed of light (Hoshino 2008). $B_z \sim 0$ is satisfied inside the filaments and the electrostatic force $-eE_x$ easily overcomes the Lorentz force $-e\beta_y B_z$ despite $E_{wake}/B_1 < 1$. Therefore, the electron is trapped by the wakefield and accelerated via the Landau resonance. The acceleration continues until the Lorentz force exceeds the electrostatic force. The bottom panel of Figure 6 shows

the total force $-e(E_x + \beta_y B_z)$ (red), electrostatic force $-eE_x$ (green), and Lorentz force $-e\beta_y B_z$ (blue) normalized by eB_1 at the electron position. The electrostatic force indeed dominates over the Lorentz force for $1795 \lesssim \omega_{pe}t \lesssim 1810$ and then the total force is controlled by the Lorentz force after $\omega_{pe}t \simeq 1810$. One may think that this process is similar to the shock surfing acceleration (SSA; Shimada & Hoshino 2000; Hoshino & Shimada 2002), in which the electrostatic waves trap the incoming electrons and the motional electric field accelerates them during the multiple reflection within the electrostatic waves. The essential difference is that the electrons gain the energies from the wakefield during the trapping because the motional electric field vanishes within the filaments $B_z \sim 0$. This acceleration mechanism is analogous to the standard WFA in laboratory plasmas rather than the SSA. We have confirmed our idea that the electrons pre-accelerated by the wakefield inside the filaments are further accelerated via the pickup process by performing the test particle simulations (see Appendix B).

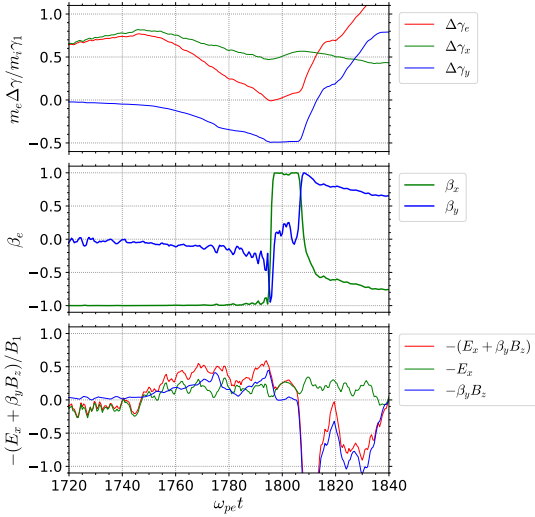


Figure 6. Time evolution of the nonthermal electron. Top panel: the energy gain $\Delta\gamma_e = \gamma_e - \gamma_1$ (red) and work done by E_x (green) and E_y (blue). Middle panel: the three velocity β_x (green) and β_y (blue). Bottom panel: the total force $-e(E_x + \beta_y B_z)$ (red), electrostatic force $-eE_x$ (green), and Lorentz force $-e\beta_y B_z$ (blue) at the electron position.

We evaluate the initial Lorentz factor γ_{0e} . Since the wakefield directly accelerates the nonthermal electron within the filaments, the energy gain is expressed as

$$\Delta\gamma_x = \frac{eE_{wake}L_{acc,e}}{m_e c^2} = \gamma_1 \sqrt{\sigma_e} \frac{E_{wake}}{B_1} \frac{L_{acc,e}}{c/\omega_{pe}}, \quad (16)$$

where E_{wake} is the wakefield amplitude and $L_{acc,e}$ is the acceleration length. E_{wake} can be estimated as (Hoshino

2008)

$$\frac{E_{wake}}{B_1} = \frac{1}{\gamma_1 \sqrt{\sigma_e}} \frac{\eta a^2}{\sqrt{1 + \eta a^2}} \sim \sqrt{\frac{\epsilon_p}{\sigma_e}}, \quad (17)$$

where η represents the wave polarization: $\eta = 1$ for circular polarization and $\eta = 1/2$ for linear polarization. Here we have used Equation 4 and $\eta = 1/2$, and neglected factors on the order of unity. By substituting $\epsilon_p \sim 1$ and $\sigma_e = 5$ into Equation 17, we obtain $E_{wake}/B_1 \sim O(10^{-1})$, which agrees with our simulation results (see Figure 2). The acceleration length corresponds to the wakefield wavelength for the WFA in laboratory plasmas. In our shock simulations, however, the acceleration length is limited by the size of the unmagnetized region which is much smaller than the wakefield wavelength. We evaluate $L_{acc,e}$ from the nonthermal electron trajectories in Figure 5:

$$\frac{L_{acc,e}}{c/\omega_{pe}} \sim 10. \quad (18)$$

By substituting Equations 17 and 18 into Equation 16, we have the estimate of the initial Lorentz factor γ_{0e} :

$$\gamma_{0e} \sim 1 + \Delta\gamma_x \sim \alpha \gamma_1 \sqrt{\epsilon_p}, \quad (19)$$

where

$$\alpha \equiv \frac{L_{acc,e}}{c/\omega_{pe}} \sim 10. \quad (20)$$

By substituting $\epsilon_p \sim 1$, we have $m_e \Delta\gamma_x / m_i \gamma_1 \sim \alpha \sqrt{\epsilon_p} m_e / m_i \sim O(10^{-1})$. The increase of $\Delta\gamma_x$ for $1795 \lesssim \omega_{pe}t \lesssim 1810$ is ~ 0.1 (see the top panel of Figure 6) and consistent with this estimate. We finally obtain

$$\gamma_{max,e} \sim \alpha \gamma_1^3 \sqrt{\epsilon_p} \sim \alpha \gamma_1^3. \quad (21)$$

This shows that a highly relativistic shock $\gamma_1 \gg 1$ can be an efficient particle accelerator.

Equation 21 shows the electron maximum Lorentz factor is $\gamma_{max,e} m_e / m_i \sim 10^4$ for $\gamma_1 = 40$ and $\gamma_{max,e} m_e / m_i \sim 10^6$ for $\gamma_1 = 100$. However, the electron energy spectra in Figure 3 demonstrate that the maximum Lorentz factor in our simulations is much smaller than we expect. Although the maximum Lorentz factor for $\gamma_1 = 100$ is larger than that for $\gamma_1 = 40$, the difference is at most a factor of 2. The deviation from the analytical estimate can be explained as follows. In the simulation frame, the picked-up electrons propagate towards the $-x$ direction while accelerated by the motional electric field. If they are picked up near the shock front, they enter the shock soon and the acceleration ceases before they take the maximum Lorentz factor. Equation 8 shows that the Lorentz factor takes its maximum when $\theta_e = \pi$. Equation 9 reduces to

$$x_e = x_{0e} - c\beta_1 t_{acc,e}, \quad (22)$$

where $t_{acc,e}$ is the acceleration timescale. By substituting this and $\theta_e = \pi$ into Equation 11, we can evaluate $t_{acc,e}$:

$$\omega_{ce} t_{acc,e} \sim 2\pi\gamma_1^2\gamma_{0e} \sim 2\pi\alpha\gamma_1^3, \quad (23)$$

We finally obtain the moving distance of the electron in the x direction $\Delta x_e = |x_e - x_{0e}|$ during the time period $\Delta t = t_{acc,e}$:

$$\frac{\Delta x_e}{c/\omega_{pe}} = \beta_1\omega_{pe}t_{acc,e} \sim \frac{2\pi\alpha\gamma_1^3}{\sqrt{\sigma_e}}. \quad (24)$$

This estimate shows $\Delta x_e/(c/\omega_{pe}) \sim 10^6$ for $\gamma_1 = 40$ and $\Delta x_e/(c/\omega_{pe}) \sim 10^7$ for $\gamma_1 = 100$, which are much larger than the precursor wave region: $1100 \lesssim x/(c/\omega_{pe}) \lesssim 1800$ in the final state of our simulations. Therefore, the picked-up electrons enter the shock before they obtain the theoretical maximum Lorentz factor. Since the group velocity of the precursor wave $v_g \sim c$ is faster than the shock propagation velocity $v_{sh} \sim (1/2 + 3\sigma_i/4)c \sim 0.575c$, the precursor wave region becomes larger as time passes. In the later phase, the incoming electrons can be picked up far away from the shock front and sufficiently accelerated by the motional electric field before entering the shock. We thus think that the observed Lorentz factor will be closer to the theoretical one if we follow the long-term evolution. Our test-particle simulations indeed demonstrate that the maximum Lorentz factor is consistent with the above estimate (see Appendix B). These results indicate that the particle energy spectra do not reach the steady state yet. Nonthermal tails might be observed in the downstream in the later phase.

5.2. Ion acceleration

The ion acceleration can be explained by the pickup process as well. Figure 7 shows the nonthermal and thermal ion trajectories in the same format as Figure 4. The thermal ion is oscillating inside the wakefield, whereas the nonthermal ion is accelerated by the motional electric field. The analytical solutions of the pickup process (Equations 8, 9, 10, and 11) are shown in black and gives a good agreement with the simulation results.

We here discuss how ions are injected into the pickup process. Figure 8 shows the trajectories of nonthermal (gray) and thermal (green) ions with the magnetic field \tilde{B}_z which is determined from the snapshot at $\omega_{pe}t = 1660$ in the same manner as for the electron. The ion injection occurs in highly magnetized region $B_z/B_1 > 1$ unlike the electron. The incoming cold ions are gradually thermalized by the SRS and/or the FI, which is clearly seen in the phase space density plots of Figure 2. The thermalized ones can be slightly deviated from the bulk motion and $E \times B$ drift can be

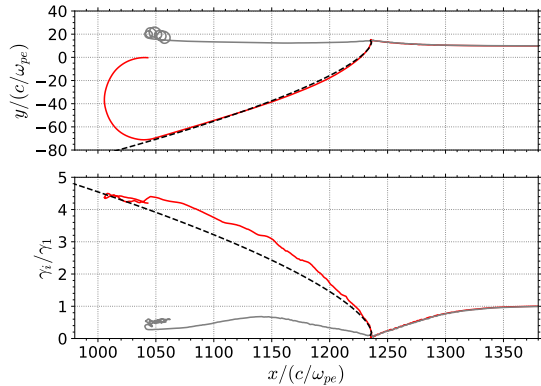


Figure 7. Ion trajectories in the same format as Figure 4

induced. The ion's trajectory is thus given by the cycloid, which is the case for the thermal ions (green lines). On the other hand, the nonthermal ones (gray lines) are suddenly reflected toward the $+x$ direction during the cycloid motion and then picked up by the bulk flow. This kick toward upstream seems to trigger the pickup process.

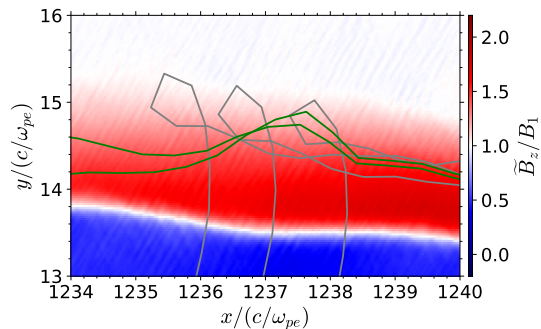


Figure 8. Trajectories of the nonthermal (gray) and thermal (green) ions with \tilde{B}_z at $\omega_{pe}t = 1660$.

Figure 9 displays the time evolution of the typical nonthermal (left) and thermal (right) ions in the same format as Figure 6. We take the moving average for the time period $\omega_{pe}\Delta t = 5$ as well. The energy gain $\Delta\gamma_i = \gamma_i - \gamma_1$ (red) and work done by E_x (green) and E_y (blue) normalized by γ_1 are shown in the top panels. In the case of the nonthermal ions (left), both the wakefield and the motional electric field contribute to the energy loss for $\omega_{pe}t \lesssim 1669$. $\Delta\gamma_i$ increases in time after $\omega_{pe}t \sim 1669$ and $\Delta\gamma_y$ exhibits the same tendency, indicating that the ion enters the pickup process at $\omega_{pe}t \sim 1669$. As can be seen in the left middle panel, at $\omega_{pe}t \sim 1669$, β_x becomes positive and the ion decoupling occurs. The left bottom panel of Figure 6 demonstrates that the electrostatic force eE_x (green) exceeds the Lorentz force $e\beta_y B_z$ (blue) for $1668 \lesssim \omega_{pe}t \lesssim 1669$

and the wakefield can reflect the incoming ion. We think that the kick imparted by the wakefield determines whether the ion enters the pickup process or not. The drifting ions can satisfy $\beta_y \sim 0$ at some point on the way to the shock. If the wakefield kicks them at the time when $\beta_y \sim 0$ is satisfied, the electrostatic force eE_x can easily overcome the Lorentz force $e\beta_y B_z \sim 0$. Furthermore, the Lorentz factor of the drifting ions has the minimum value when $\beta_y \sim 0$ and they are relatively subject to the wakefield. In fact, the thermal ion (right) shows that the eE_x is negative at the time $\omega_{pe}t \sim 1670$ when $\beta_y \sim 0$ is satisfied and the wakefield cannot reflect it. Although the increase of $\Delta\gamma_x$ is barely visible for $1668 \lesssim \omega_{pe}t \lesssim 1669$ in the left top panel, we think the finite kick imparted by the wakefield is responsible for the decoupling.

The ion injection into the pickup process seems to be different from the electron. This may be attributed to the mass difference like the standard WFA in laboratory plasmas. Electrons are relatively easily accelerated by the wakefield whose phase velocity is almost equal to the speed of light via the Landau resonance, whereas ions have difficulty with the resonance due to the large mass. Our simulations indeed demonstrate the efficient electron WFA inside the filaments. Although the ion WFA is transient and inefficient, we think that this finite pre-acceleration injects ions into the pickup process.

We here evaluate the ion maximum Lorentz factor $\gamma_{max,i}$ in the same manner as for the electron. Since the incoming ion is reflected by the wakefield, $\Delta\gamma_x$ can be written as

$$\Delta\gamma_x = \frac{eE_{wake}L_{acc,i}}{m_i c^2} \sim \frac{m_e}{m_i} \gamma_1 \sqrt{\epsilon_p} \frac{L_{acc,i}}{c/\omega_{pe}}. \quad (25)$$

The nonthermal ion trajectories in Figure 8 indicate

$$\frac{L_{acc,i}}{c/\omega_{pe}} \sim 1. \quad (26)$$

γ_{0i} can be estimated as

$$\gamma_{0i} \sim 1 + \Delta\gamma_x \sim 1 + \frac{m_e}{m_i} \gamma_1 \sqrt{\epsilon_p} \quad (27)$$

The ion maximum Lorentz factor $\gamma_{max,i}$ can be derived from Equation 12,

$$\gamma_{max,i} \sim \left(1 + \frac{m_e}{m_i} \gamma_1 \sqrt{\epsilon_p}\right) \gamma_1^2 \sim \left(1 + \frac{m_e}{m_i} \gamma_1\right) \gamma_1^2 \quad (28)$$

Here we have used $\epsilon_p \sim 1$. As can be seen in Figure 3, the ion energy spectra show the smaller maximum Lorentz factor due to the time dilation. We can estimate the moving distance in the x direction during the

acceleration as in the case of the electron. The acceleration timescale $t_{acc,i}$ is expressed as

$$\omega_{ci} t_{acc,i} \sim 2\pi \left(1 + \frac{m_e}{m_i} \gamma_1\right) \gamma_1^2. \quad (29)$$

We obtain the moving distance of the ion in the x direction $\Delta x_i = |x_i - x_{0i}|$:

$$\frac{\Delta x_i}{c/\omega_{pe}} = \beta_1 \omega_{pe} t_{acc,i} \sim \frac{2\pi (m_i/m_e + \gamma_1) \gamma_1^2}{\sqrt{\sigma_e}}. \quad (30)$$

This estimate gives $\Delta x_i/(c/\omega_{pe}) \sim 10^5$ for $\gamma_1 = 40$ and $\sim 10^6$ for $\gamma_1 = 100$ and thus the pickup ions enter the shock before they reach the maximum Lorentz factor in our simulations. Nonthermal ions as well as electrons might be seen in the downstream in the later phase.

6. DISCUSSION

In this work, we assumed the precursor wave power $\epsilon_p \sim 1$ which is valid for $\sigma_i \sim 0.1 - 1$ (Iwamoto et al. 2019). ϵ_p is independent of γ_1 as long as $\gamma_1 \gg 1$ (Plotnikov & Sironi 2019) and it is mainly controlled by σ_i due to the ion-electron coupling (Lyubarsky 2006; Hoshino 2008; Iwamoto et al. 2019). Although the σ_i dependence is not fully understood, previous PIC simulations demonstrated that ϵ_p is convex upward as a function of σ_i and takes the maximum value $\epsilon_p \sim 1$ at $\sigma_i \sim 0.1$. The ion acceleration efficiency (Equation 28) is not strongly dependent on ϵ_p as long as $\gamma_1 < m_i/m_e$ and $\gamma_{max,i} \sim \gamma_1^2$ for $\epsilon_p \ll 1$. On the other hand, the electron acceleration efficiency (Equation 21) drastically deteriorates for $\epsilon_p \ll 1$ and may be reduced to $\gamma_{max,e} \sim \gamma_{max,i} \sim \gamma_1^2$. For low σ_i , however, the electron acceleration is not necessarily less efficient. The acceleration length $L_{acc,e}$ may be much greater because $E_{wake}/B_1 \sim \delta B/B_1 > 1$ can be satisfied for weakly magnetized plasmas and the electrostatic force can easily exceed the Lorentz force. The acceleration length may be comparable to the wakefield wavelength (Kruer 1988; Hoshino 2008),

$$\alpha = \frac{L_{acc,e}}{c/\omega_{pe}} \sim \gamma_1. \quad (31)$$

The maximum Lorentz factor is expressed as

$$\gamma_{max,e} \sim \gamma_1^4 \sqrt{\epsilon_p}. \quad (32)$$

The Weibel instability develops for $\sigma_i \ll 1$ and the wave power declines because the ring-like momentum distribution in the shock-transition which is essential for the SMI is strongly modified by the Weibel-generated magnetic field (Sironi & Spitkovsky 2011; Iwamoto et al. 2017, 2018). However, Equation 32 exhibits the weak

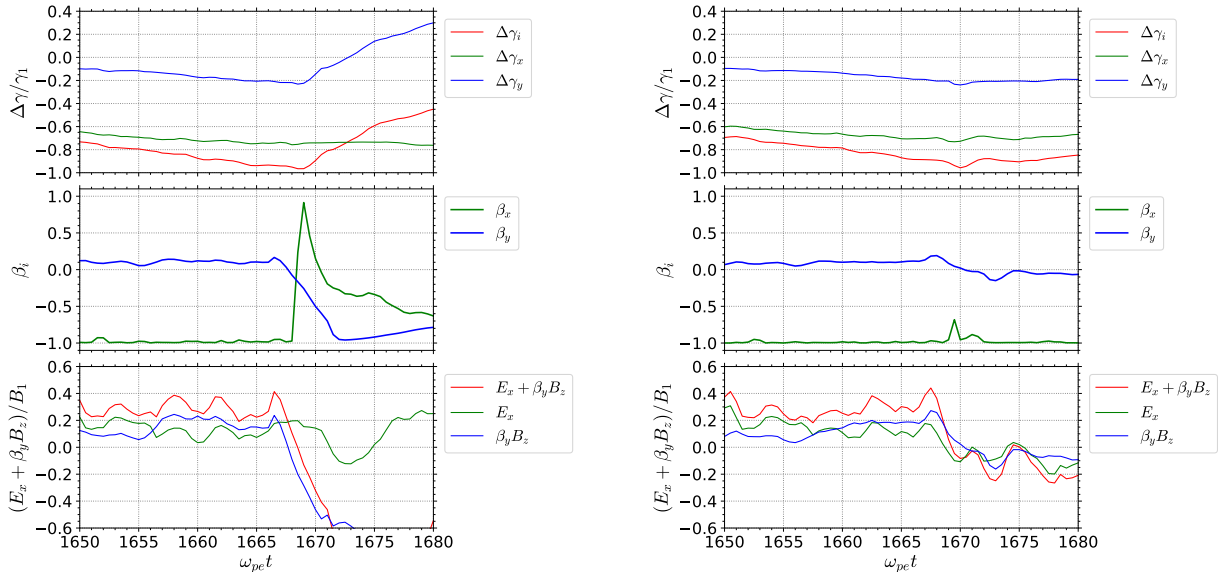


Figure 9. Time evolution of the nonthermal (left) and thermal (right) ion in the same format as Figure 6

dependence on ϵ_p compared to γ_1 . We thus speculate that the efficient electron acceleration occurs as long as $\gamma_1 \gg 1$.

The upstream temperature has an influence on the acceleration efficiency as well. Since the accelerated/heated particles enter the shock, ϵ_p may decrease in time due to the suppression of the higher-order harmonics (Amato & Arons 2006). In pair plasma, Babul & Sironi (2020) reported that the wave emission efficiency declines by almost two orders of magnitude for the thermal spread $k_B T_e / m_e c^2 \gtrsim 10^{-1}$. Although the temperature dependence in ion-electron plasmas remains unsolved, ϵ_p probably shows the similar tendency. The precursor wave emission might cease and the size of the precursor wave region might be insufficient to accelerate the incoming particles up to the theoretical estimate even if we follow the long-term evolution. The particle energy spectra in the final state is an open question.

Both electrons and ions are accelerated via the pickup process in the upstream. We speculate that the pickup process provides seed particles for other acceleration mechanisms such as Fermi acceleration. The pre-accelerated particles in the upstream may be further accelerated and power-law spectra may be generated in the downstream.

The pre-existing cosmic rays may be re-accelerated by the pickup process. Such energetic protons can diffuse far upstream. Since they are decoupled from the upstream bulk flow, the pickup process can work. According to Equation 12, they can be re-accelerated by a factor of γ_1^2 . This re-acceleration process may repeatedly operate and they may be accelerated up to the UHECR energy range.

7. SUMMARY

We investigated the particle acceleration in relativistic ion-electron shocks by 2D PIC simulations. The particle energy spectra in the upstream show the nonthermal tails for both electrons and ions. We found that they are mainly accelerated by the motional electric field. This particle acceleration is well-described by the pickup process, in which particles are once decoupled from the upstream bulk flow by the wakefield, and are picked up again by the flow. We estimated the maximum Lorentz factor $\gamma_{max,e} \sim \alpha \gamma_1^3$ for the electron and $\gamma_{max,i} \sim (1 + m_e \gamma_1 / m_i) \gamma_1^2$ for the ion, where $\alpha \sim 10$ is the normalized acceleration length and determined from our simulations. Since this acceleration requires a large computational domain, we could not follow the whole acceleration process due to the limitation of the computational resources. The accelerated particles might exhibit a power-law-like spectra in the downstream in a later phase. The pickup process may play a significant role for particle acceleration in highly relativistic shocks $\gamma_1 \gg 1$ such as external shocks of GRBs.

ACKNOWLEDGMENTS

We are grateful to Jacek Niemiec, Martin Pohl, Oleh Kobzar, Arianna Ligorini, and Artem Bohdan for fruitful discussions.

This work is supported by JSPS KAKENHI grant No. 20J00280 and 20KK0064.

This work used the computational resources of the HPCI system provided by Information Technology Cen-

ter, Nagoya University through the HPCI System Research Project (Project ID: hp200035, hp210154).

Numerical computations were in part carried out on Cray XC50 at Center for Computational Astrophysics, National Astronomical Observatory of Japan.

APPENDIX

A. ANALYTICAL SOLUTIONS OF PICKUP PROCESS

We here derive the analytical solutions of the pickup process. Let us assume a charged particle in the background magnetic field $B_z = B_1$ and the motional electric field $E_y = -\beta_1 B_1$. The basic equations are the relativistic equations of motion:

$$m_s c \frac{du_{xs}}{dt} = q_s \beta_{ys} B_1, \quad (\text{A1})$$

$$m_s c \frac{du_{ys}}{dt} = -q_s (\beta_{xs} + \beta_1) B_1. \quad (\text{A2})$$

where $\mathbf{u}_s = \gamma_s \boldsymbol{\beta}_s$ is the four velocity, $q_e = -e$ is the electron charge, and $q_i = +e$ is the ion charge. By performing Lorentz transformation from the simulation frame into the plasma rest frame, Equations A1 and A2 reduce to

$$m_s c \frac{du'_{xs}}{dt'} = q_s \beta'_{ys} B'_1 \quad (\text{A3})$$

$$m_s c \frac{du'_{ys}}{dt'} = -q_s \beta'_{xs} B'_1, \quad (\text{A4})$$

where the prime indicates the physical quantities in the plasma rest frame. The motional electric field vanishes in the plasma rest frame and thus the kinetic energy is conserved:

$$\gamma'_s = \text{const.} = \gamma_1 \gamma_{0s} (1 + \beta_1 \beta_{0s}), \quad (\text{A5})$$

where $\gamma_{0s} = 1/\sqrt{1 - \beta_{0s}^2}$ is the initial Lorentz factor at $t = 0$. Here we have assumed the initial three velocity $\boldsymbol{\beta}_{0s} = \beta_{0s} \hat{\mathbf{x}}$ and performed the Lorentz transformation $\gamma'_s = \gamma_1 \gamma_s (1 + \beta_1 \beta_{xs})$. Equations A3 and A4 describe the gyromotion around the background magnetic field $B'_1 = B_1/\gamma_1$ and are easily solved:

$$u'_{xs} = u'_{0s} \cos \theta'_s, \quad (\text{A6})$$

$$u'_{ys} = \pm u'_{0s} \sin \theta'_s, \quad (\text{A7})$$

$$x'_s = x'_{0s} + u'_{0s} \frac{c}{\omega_{cs}} \sin \theta'_s, \quad (\text{A8})$$

$$y'_s = y'_{0s} \pm u'_{0s} \frac{c}{\omega_{cs}} (1 - \cos \theta'_s), \quad (\text{A9})$$

$$\theta'_s = \frac{\omega_{cs} t'}{\gamma'_s}, \quad (\text{A10})$$

$$u'_{0s} = \gamma_1 \gamma_{0s} (\beta_1 + \beta_{0s}), \quad (\text{A11})$$

where the subscript 0 represents the initial quantities at $t = 0$. The positive (negative) sign corresponds to

the electron (ion). Note that $\omega_{cs} = eB_1/\gamma_1 m_s c$ is the unsigned cyclotron frequency. By performing Lorentz transformation from the plasma rest frame into the simulation frame, we obtain the exact solutions of Equations A1 and A2:

$$\gamma_s = \gamma_1^2 \gamma_{0s} [(1 + \beta_1 \beta_{0s}) - \beta_1 (\beta_1 + \beta_{0s}) \cos \theta_s], \quad (\text{A12})$$

$$u_{xs} = \gamma_1^2 \gamma_{0s} [-\beta_1 (1 + \beta_1 \beta_{0s}) + (\beta_1 + \beta_{0s}) \cos \theta_s], \quad (\text{A13})$$

$$u_{ys} = \pm \gamma_1 \gamma_{0s} (\beta_1 + \beta_{0s}) \sin \theta_s, \quad (\text{A14})$$

$$x_s = x_{0s} - c \beta_1 t + \gamma_{0s} (\beta_1 + \beta_{0s}) \frac{c}{\omega_{cs}} \sin \theta_s, \quad (\text{A15})$$

$$y_s = y_{0s} \pm \gamma_1 \gamma_{0s} (\beta_1 + \beta_{0s}) \frac{c}{\omega_{cs}} (1 - \cos \theta_s), \quad (\text{A16})$$

$$\theta_s = \frac{\omega_{cs} [t + \beta_1 (x_s - x_{0s})/c]}{\gamma_{0s} (1 + \beta_1 \beta_{0s})}. \quad (\text{A17})$$

By numerically solving Equations A15 and A17, we can determine x_s and θ_s and finally obtain the theoretical solutions of the pickup process.

B. TEST PARTICLE SIMULATION

To confirm that the transverse filamentary structures triggers the pickup process, we perform the test particle simulations. The particle pusher proposed by Vay (2008) is applied to this test particle code. We consider the ambient magnetic field B_1 , the motional electric field $E_y = -\beta_1 B_1$, the wakefield, and the filaments. The wakefield and filaments are modeled as

$$E_x = \begin{cases} -E_{wake} \sin \left[\frac{2\pi}{\lambda_{wake}} (x - ct) \right] & (x < ct) \\ 0 & (x \geq ct) \end{cases}, \quad (\text{B18})$$

$$B_z = B_1 + B_f \sin \left(\frac{2\pi}{\lambda_f} y \right), \quad (\text{B19})$$

$$E_y = -\beta_1 B_z, \quad (\text{B20})$$

where E_{wake} is the wakefield amplitude, λ_{wake} is the wakefield wavelength, B_f is the filament amplitude, and λ_f is the filament wavelength. Particles are injected at $x = 0$ toward the $-x$ direction with the bulk Lorentz factor $\gamma_1 = 40$. The thermal velocity of the injected plasma flow in the plasma rest frame is $\beta_{th} = 0.1$. Based on our PIC simulation results, we determined $E_{wake}/B_1 = 0.2$, $\lambda_{wake}/(c/\omega_{pe}) = 500$, $B_f/B_1 = 1$, and $\lambda_f/(c/\omega_{pe}) = 15$. The other parameters are identical to our PIC simulations.

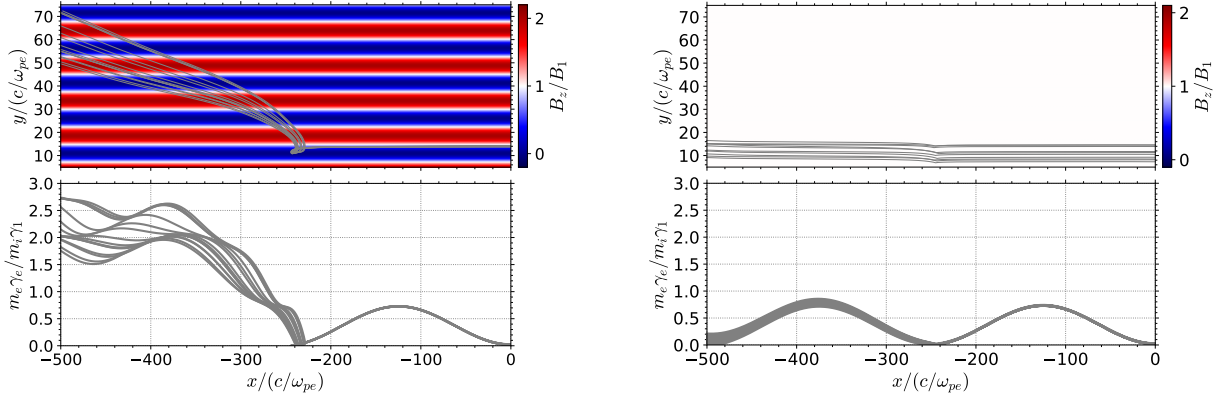


Figure 10. Electron trajectories with (left) and without (right) the filaments.

Figure 10 show the trajectories of the energetic electrons in x - y space (top) and x - γ space (bottom). The color maps represent B_z in the case of $B_f = 1$ (left) and $B_f = 0$ (right). The incoming electrons are picked up at $x/(c/\omega_{pe}) \sim -220$ for $B_f = 1$, whereas they are merely oscillating inside the wakefield for $B_f = 0$. The trajectories give a clear proof that the filaments are essential for entering the pickup process.

Figure 11 displays the enlarged view of the top-left panel of Figure 10. The incoming electrons enter the unmagnetized region arising from the filaments and then they are picked up by the bulk flow. The filaments obviously triggers the pickup process as in the case with our PIC simulations.

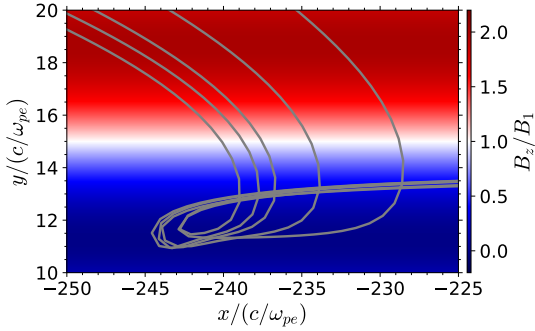


Figure 11. Trajectories of the energetic electrons with the magnetic field B_z .

Figure 12 shows the time evolution of the typical energetic electron in the same format as Figure 6. The time evolution in our test particle simulation exhibit the qualitatively same behavior as that in our PIC simulation. The incoming electron is first decelerated by the wakefield and begins to gyrate. The motional electric field as well as the wakefield then decelerates it for $210 \lesssim \omega_{pe}t \lesssim 244$. The increase of $\Delta\gamma_x$ and the positive velocity $\beta_x \sim 1$ for $244 \lesssim \omega_{pe}t \lesssim 256$ shows that the

electrons are accelerated by the wakefield via the Landau resonance. The electrostatic force dominates over the Lorentz force for $244 \lesssim \omega_{pe}t \lesssim 256$ and thus the Landau resonance can work. After $\omega_{pe}t \simeq 256$, $\Delta\gamma_y$ becomes dominant and the electron enters the pickup process. The Lorentz force indeed exceeds the electrostatic force after $\omega_{pe}t \simeq 256$. The electron is detrapped from the wakefield and then picked up by the bulk flow.

The injection into the pickup process is well-described by this toy model. We thus think that the filaments trigger the pickup process.

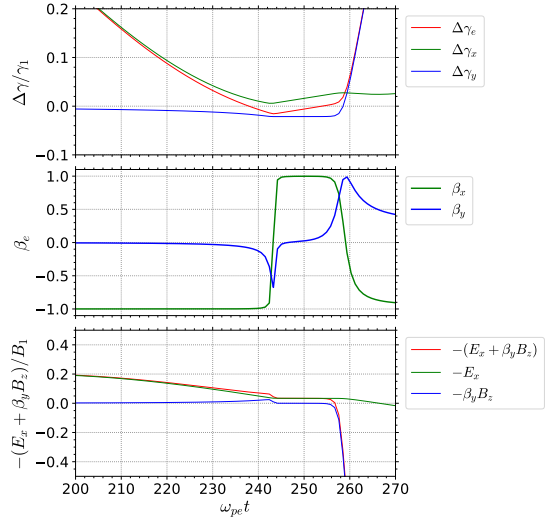


Figure 12. Time evolution of the typical energetic electron in the same format as Figure 6

Figure 13 shows the time evolution of the ion Lorentz factor. The maximum Lorentz factor is $\gamma_{max,e} \sim \alpha\gamma_1^3$ and the acceleration timescale is $\omega_{ce}t \sim 2\pi\alpha\gamma_1^3$. This result is consistent with the theoretical estimate discussed in the main text, indicating that the pickup particles can be accelerated up to the theoretical maximum Lorentz

factor in the shock system if the size of the precursor wave region is sufficiently large.

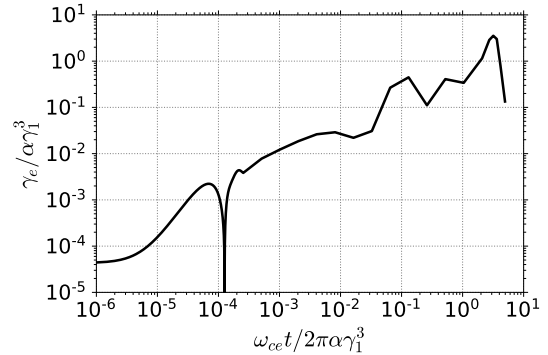


Figure 13. Time evolution of the Lorentz factor.

REFERENCES

- Aab, A., Abreu, P., Aglietta, M., et al. 2018, *ApJL*, 853, L29, doi: [10.3847/2041-8213/aaa66d](https://doi.org/10.3847/2041-8213/aaa66d)
- Aartsen, M. G., Ackermann, M., Adams, J., et al. 2018, *Sci*, 361, 147, doi: [10.1126/science.aat2890](https://doi.org/10.1126/science.aat2890)
- Amato, E., & Arons, J. 2006, *ApJ*, 653, 325, doi: [10.1086/508050](https://doi.org/10.1086/508050)
- Arons, J. 2003, *ApJ*, 589, 871, doi: [10.1086/374776](https://doi.org/10.1086/374776)
- Babul, A.-N., & Sironi, L. 2020, *MNRAS*, 499, 2884, doi: [10.1093/mnras/staa2612](https://doi.org/10.1093/mnras/staa2612)
- Beloborodov, A. M. 2017, *ApJL*, 843, L26, doi: [10.3847/2041-8213/aa78f3](https://doi.org/10.3847/2041-8213/aa78f3)
- . 2020, *ApJ*, 896, 142, doi: [10.3847/1538-4357/ab83eb](https://doi.org/10.3847/1538-4357/ab83eb)
- Blandford, R., Meier, D., & Readhead, A. 2019, *ARA&A*, 57, 467, doi: [10.1146/annurev-astro-081817-051948](https://doi.org/10.1146/annurev-astro-081817-051948)
- Chen, P., Tajima, T., & Takahashi, Y. 2002, *PhRvL*, 89, 161101, doi: [10.1103/PhysRevLett.89.161101](https://doi.org/10.1103/PhysRevLett.89.161101)
- Drake, J. F., Kaw, P. K., Lee, Y. C., et al. 1974, *PhFl*, 14, 778, doi: [10.1063/1.1694789](https://doi.org/10.1063/1.1694789)
- Ebisuzaki, T., & Tajima, T. 2014, *Aph*, 56, 9, doi: [10.1016/j.astropartphys.2014.02.004](https://doi.org/10.1016/j.astropartphys.2014.02.004)
- . 2021, *Aph*, 128, 102567, doi: [10.1016/j.astropartphys.2021.102567](https://doi.org/10.1016/j.astropartphys.2021.102567)
- Fried, B. D. 1959, *PhFl*, 2, 337, doi: [10.1063/1.1705933](https://doi.org/10.1063/1.1705933)
- Gallant, Y. A., Hoshino, M., Langdon, A. B., Arons, J., & Max, C. E. 1992, *ApJ*, 391, 73, doi: [10.1086/171326](https://doi.org/10.1086/171326)
- Hillas, A. M. 1984, *ARA&A*, 22, 425, doi: [10.1146/annurev.aa.22.090184.002233](https://doi.org/10.1146/annurev.aa.22.090184.002233)
- Hoshino, M. 2008, *ApJ*, 672, 940, doi: [10.1086/523665](https://doi.org/10.1086/523665)
- Hoshino, M., & Arons, J. 1991, *PhFlB*, 3, 818, doi: [10.1063/1.859877](https://doi.org/10.1063/1.859877)
- Hoshino, M., Arons, J., Gallant, Y. A., & Langdon, A. B. 1992, *ApJ*, 390, 454, doi: [10.1086/171296](https://doi.org/10.1086/171296)
- Hoshino, M., & Shimada, N. 2002, *ApJ*, 572, 880, doi: [10.1086/340454](https://doi.org/10.1086/340454)
- Ikeya, N., & Matsumoto, Y. 2015, *PASJ*, 67, 64, doi: [10.1093/pasj/psv052](https://doi.org/10.1093/pasj/psv052)
- Iwamoto, M., Amano, T., Hoshino, M., & Matsumoto, Y. 2017, *ApJ*, 840, 52, doi: [10.3847/1538-4357/aa6d6f](https://doi.org/10.3847/1538-4357/aa6d6f)
- . 2018, *ApJ*, 858, 93, doi: [10.3847/1538-4357/aaba7a](https://doi.org/10.3847/1538-4357/aaba7a)
- Iwamoto, M., Amano, T., Hoshino, M., et al. 2019, *ApJL*, 883, L35, doi: [10.3847/2041-8213/ab4265](https://doi.org/10.3847/2041-8213/ab4265)
- Kaw, P. K., Schmid, G., & Wilcox, T. 1973, *PhFl*, 16, 1522, doi: [10.1063/1.1694552](https://doi.org/10.1063/1.1694552)
- Kruer, W. L. 1988, *The Physics of Laser Plasma Interactions*, ed. D. Pines (Boston: Addison-Wesley)
- Kuramitsu, Y., Sakawa, Y., Hoshino, M., Chen, S. H., & Takabe, H. 2012, *HEDP*, 8, 266, doi: [10.1016/j.hedp.2012.03.016](https://doi.org/10.1016/j.hedp.2012.03.016)
- Kuramitsu, Y., Sakawa, Y., Kato, T., Takabe, H., & Hoshino, M. 2008, *ApJ*, 682, 113, doi: [10.1086/591247](https://doi.org/10.1086/591247)
- Kuramitsu, Y., Nakanii, N., Kondo, K., et al. 2011a, *PhPl*, 18, 010701, doi: [10.1063/1.3528434](https://doi.org/10.1063/1.3528434)
- . 2011b, *PhRvE*, 83, 026401, doi: [10.1103/PhysRevE.83.026401](https://doi.org/10.1103/PhysRevE.83.026401)
- Langdon, A. B., Arons, J., & Max, C. E. 1988, *PhRvL*, 61, 779, doi: [10.1103/PhysRevLett.61.779](https://doi.org/10.1103/PhysRevLett.61.779)
- Ligorini, A., Niemiec, J., Kobzar, O., et al. 2021a, *MNRAS*, 501, 4837, doi: [10.1093/mnras/staa3901](https://doi.org/10.1093/mnras/staa3901)
- . 2021b, *MNRAS*, 502, 5065, doi: [10.1093/mnras/stab220](https://doi.org/10.1093/mnras/stab220)
- Liu, Y. L., Isayama, S., Chen, S. H., & Kuramitsu, Y. 2019, *HEDP*, 31, 64, doi: [10.1016/j.hedp.2019.03.004](https://doi.org/10.1016/j.hedp.2019.03.004)
- Liu, Y. L., Kuramitsu, Y., Isayama, S., & Chen, S. H. 2018, *PhPl*, 25, 013110, doi: [10.1063/1.5006325](https://doi.org/10.1063/1.5006325)
- Liu, Y. L., Kuramitsu, Y., Moritaka, T., & Chen, S. H. 2017, *HEDP*, 22, 46, doi: [10.1016/j.hedp.2017.02.006](https://doi.org/10.1016/j.hedp.2017.02.006)
- Lyubarsky, Y. 2006, *ApJ*, 652, 1297, doi: [10.1086/508606](https://doi.org/10.1086/508606)
- . 2008, *ApJ*, 682, 1443, doi: [10.1086/589435](https://doi.org/10.1086/589435)
- . 2014, *MNRAS*, 442, L9, doi: [10.1093/mnras/llu046](https://doi.org/10.1093/mnras/llu046)

- . 2018, MNRAS, 474, 1135, doi: [10.1093/mnras/stx2832](https://doi.org/10.1093/mnras/stx2832)
- . 2019, MNRAS, 490, 1474, doi: [10.1093/mnras/stz2712](https://doi.org/10.1093/mnras/stz2712)
- Margalit, B., Beniamini, P., Sridhar, N., & Metzger, B. D. 2020, ApJL, 899, L27, doi: [10.3847/2041-8213/abac57](https://doi.org/10.3847/2041-8213/abac57)
- Matsumoto, Y., Amano, T., & Hoshino, M. 2013, PhRvL, 111, 215003, doi: [10.1103/PhysRevLett.111.215003](https://doi.org/10.1103/PhysRevLett.111.215003)
- Matsumoto, Y., Amano, T., Kato, T. N., & Hoshino, M. 2015, Sci, 347, 974, doi: [10.1126/science.1260168](https://doi.org/10.1126/science.1260168)
- Max, C. E., Arons, J., & Langdon, A. B. 1974, PhRvL, 33, 209, doi: [10.1103/PhysRevLett.33.209](https://doi.org/10.1103/PhysRevLett.33.209)
- Melrose, D. B. 2017, RvMPP, 1, 5, doi: [10.1007/s41614-017-0007-0](https://doi.org/10.1007/s41614-017-0007-0)
- Metzger, B. D., Margalit, B., & Sironi, L. 2019, MNRAS, 485, 4091, doi: [10.1093/mnras/stz700](https://doi.org/10.1093/mnras/stz700)
- Möbius, E., Hovestadt, D., Klecker, B., et al. 1985, Nature, 318, 426, doi: [10.1038/318426a0](https://doi.org/10.1038/318426a0)
- Murase, K., Mészáros, P., & Zhang, B. 2009, PhRvD, 79, 103001, doi: [10.1103/PhysRevD.79.103001](https://doi.org/10.1103/PhysRevD.79.103001)
- Oka, M., Terasawa, T., Noda, H., Saito, Y., & Mukai, T. 2002, GeoRL, 29, 1612, doi: [10.1029/2002GL015111](https://doi.org/10.1029/2002GL015111)
- Piran, T. 2005, RvMP, 76, 1143, doi: [10.1103/RevModPhys.76.1143](https://doi.org/10.1103/RevModPhys.76.1143)
- Plotnikov, I., Grassi, A., & Grech, M. 2018, MNRAS, 477, 5238, doi: [10.1093/mnras/sty979](https://doi.org/10.1093/mnras/sty979)
- Plotnikov, I., & Sironi, L. 2019, MNRAS, 485, 3816, doi: [10.1093/mnras/stz640](https://doi.org/10.1093/mnras/stz640)
- Shimada, N., & Hoshino, M. 2000, ApJL, 543, L67, doi: [10.1086/318161](https://doi.org/10.1086/318161)
- Sironi, L., Plotnikov, I., Nättilä, J., & Beloborodov, A. M. 2021, PhRvL, 127, 035101, doi: [10.1103/PhysRevLett.127.035101](https://doi.org/10.1103/PhysRevLett.127.035101)
- Sironi, L., & Spitkovsky, A. 2011, ApJ, 726, 75, doi: [10.1088/0004-637X/726/2/75](https://doi.org/10.1088/0004-637X/726/2/75)
- Sironi, L., Spitkovsky, A., & Arons, J. 2013, ApJ, 771, 54, doi: [10.1088/0004-637X/771/1/54](https://doi.org/10.1088/0004-637X/771/1/54)
- Sobacchi, E., Lyubarsky, Y., Beloborodov, A. M., & Sironi, L. 2020, MNRAS, 500, 272, doi: [10.1093/mnras/staa3248](https://doi.org/10.1093/mnras/staa3248)
- Spitkovsky, A. 2005, in AIP Conf. Proc., Vol. 801, Astrophysical Source of High Energy Particles and Radiation, ed. T. Bulik, B. Rudak, & G. Madejski (Melville, NY: AIP), 345–350, doi: [10.1063/1.2141897](https://doi.org/10.1063/1.2141897)
- Tajima, T., & Dawson, J. M. 1979, PhRvL, 43, 267, doi: [10.1103/PhysRevLett.43.267](https://doi.org/10.1103/PhysRevLett.43.267)
- Vay, J.-L. 2008, PhPl, 15, 056701, doi: [10.1063/1.2837054](https://doi.org/10.1063/1.2837054)
- Weibel, Erich, S. 1959, PhRvL, 2, 83, doi: [10.1103/PhysRevLett.2.83](https://doi.org/10.1103/PhysRevLett.2.83)